An Improved Theoretical Process-Zone Model for Delayed Hydride Cracking Initiation at a Blunt V-Notch

Yifan Huang, R.K.N.D. Rajapakse*

School of Engineering Science, Simon Fraser University, 8888 University Drive, Burnaby, British Columbia V5A 1S6, Canada
*: Corresponding author, Email: rajapakse@sfu.ca

Abstract: Delayed hydride cracking (DHC) is an important concern for pressure tubes used in nuclear reactors. In this paper, an improved analytical process-zone model is developed based on the deformation fracture criteria. A V-notch with rounded root, which is widely adopted in mechanical testing of DHC, is considered and the proposed model includes the effect of both notch angle and tip radius. Comparisons with experiments show that the proposed model has a prediction accuracy closer to the current engineering process-zone model but with slightly less conservatism. The model is extended to account for plasticity and constraint effects at the flaw tip by introducing an empirical factor that depends on key material and geometric parameters.

Keywords: Delayed hydride cracking (DHC); fracture mechanics; plasticity; process-zone; stress intensity factor

Nomenclature

a	flaw depth or crack length
E	elastic modulus
C_δ	elastic-plastic correction factor in Eq. (30)
G_c	work of separation
G_c^*	modified G_c for the elastic-plastic process zone
G^{hyd}_{Ic}	critical energy release rate for hydrided materials
K_{eff}	effective stress intensity factor in Eq. (26)
K_I	stress intensity factor for cracks
K^{hyd}_{Ic}	fracture toughness for hydrided materials
K^V_I	generalized sharp notch stress intensity factor
$K^V_{\rho,I}$	generalized blunt notch stress intensity factor
K_{IH}	isothermal threshold SIF associated with the onset of DHC
K_{IH}^*	modified K_{IH} for the elastic-plastic process zone
k_t	stress concentration factor
l_Y	length of the plasticity band
p_c	cohesive strength in the process zone model
p_H	normal stress in the process zone
R_I	stress rounding factor
r, θ	polar coordinates with origin at the sharp notch tip
s	length of process zone
W	specimen thickness
α	half of the solid wedge angle
β	half of the notch opening angle
γ	dimensionless load
γ_{TH}	threshold value of γ
δ^{hyd}_{Ic}	critical crack tip opening displacement for hydrided materials
δ_T	flaw tip opening displacement
$\tilde{\delta}_T$	dimensionless notch-tip opening displacement
δ_{Tc}	critical crack/flaw tip opening displacement
$\delta_{T\sigma n}, \delta_{T\sigma c}$	components of δ_T caused by the far-field nominal stress and cohesive stress

δ_y	opening displacement corresponding to the additional process zone that accounts for the effect of prior plastic relaxation
ν	Poisson's ratio
ξ	empirical factor in the plasticity model
ρ	root radius of the blunt flaw tip
σ_c	uniform cohesive stress
σ_n	applied nominal stress remote from the flaw
σ_p	peak flaw tip stress
σ_{pTH}	threshold peak flaw tip stress for delayed hydride cracking initiation
σ_{yc}	tensile stress in the additional process zone
σ_{YS}	material yield strength
$\sigma_{\theta\theta}$, σ_{rr}, $\tau_{r\theta}$	components of the stress tensor
ψ, ψ^*	dimensionless loading parameters

1. Introduction

Zr-2.5Nb alloy pressure tubes are an important component of the core of a CANada Deuterium Uranium (CANDU) reactor. These tubes are prone to failure by a stable and time-dependent crack growth mechanism called Delayed Hydride Cracking (DHC) which is caused by the presence of hydrogen and subsequent formation of brittle zirconium hydrides [1]. High levels of hydrogen equivalent concentration in the main body of pressure tubes are a result of deuterium pickup during service from a corrosion reaction. Manufacturing of pressure tubes also introduces hydrogen as an impurity element. Hydrogen can diffuse to a high stress concentration region, such as a service-induced flaw in pressure tubes under operating stress, and further develop a hydrided region at a flaw tip [1]. Under suitable conditions, a hydrided region may fracture and is deemed to be the initiation of DHC. Crack extension is driven by the DHC growth mechanism, which is a repetitive process of hydride formation and fracture [2-3].

One important procedure in the integrity assessment of CANDU pressure tubes is to evaluate the likelihood of DHC initiation from service-induced flaws, such as fuel bundle scratches, fuel bundle bearing pad fretting flaws, and debris fretting flaws [4]. Such fitness-for-service assessment requires abundant experimental data obtained from pressure tube materials as well as a thorough understanding of the DHC mechanisms. For simplicity, the initial approach in the assessment is to treat the flaws as sharp cracks such as those produced by fatigue pre-cracking [5]. However, real flaws in pressure tubes are usually blunt and have finite root radii. The application of the acceptance criteria developed based on sharp cracks to evaluate real blunt flaws may lead to overly conservative estimates of the allowable operation load or service life of tubes, and the consequent cost penalties. Therefore, the subsequent industry Fitness-for-Service-Guidelines (FFSG) [6] developed the acceptance criteria for evaluating DHC initiation in Zr-2.5Nb pressure tubes based on experimental data corresponding to blunt flaws with finite root radii.

Smith [7-9] and Scarth and Smith [10-11] further improved the flaw evaluation methodology by introducing a "process-zone model" to simulate the hydride region ahead of a flaw tip. The process-zone model takes into account the effect of flaw geometry and stress relaxation due to hydride formation, which are not considered in the FFSG acceptance criteria. The process-zone methodology can be further classified into two subsets, namely theoretical process-zone (TPZ) model [7-9] and engineering process-zone (EPZ) model [10-12]. The former model is thoroughly developed based on analytical solutions whereas the latter model more or less requires finite element models or parametric solutions for the stress field. The EPZ methodology has been implemented into the first version of Canadian Standards Association (CSA) Standard N285.8-15 [12] for the assessment of DHC initiation in Zr-2.5Nb pressure tubes. Reasonable agreement was observed between the experimental data [13-15] and model predictions on the threshold conditions for cracking in samples with different notch geometries.

It is noted that the emphasis of the previous analytical studies invovling the TPZ models [7-9] are on a blunt flaw in the shape of semi-ellipses or intrusions, whereas it is more common to use specimen containing a V-shaped notch with rounded root in the DHC initiation tests (e.g. [13-15]). The existing EPZ methods [10,11] for prediction of DHC initiation at such V-shaped flaws require the stress field directly obtained from a finite element model or access to parametric solutions for stress field [12]. EPZ models also require iterations as part of the solution process. On the other hand, if TPZ models could be improved to include both sharp and blunt V-shaped notches, it would provide an efficient alternative to the EPZ models and a good analytical basis to compare the EPZ solutions. The analytical solution for the stress field of a body containing a blunt V-notch has been well-established in the literature (e.g. [16-25]). Specifically, Savruk and Kazberuk [22, 23] proposed a deformation fracture criteria for sharp and blunt V-notches based on analytical stress solutions. The objective of this paper is to extend the TPZ method for V-shaped notches (sharp and blunt) by making use of the stress field and

fracture criteria given in Refs. [22,23] and include the notch tip constraint and plasticity effects in the improved TPZ model.

2. Process-zone Methodology and Smith's TPZ Model

Figure 1 shows the schematic of the process-zone model proposed by Smith [7-9] and Scarth and Smith [10-12]. A blunt flaw in a two-dimensional (2D) semi-infinite solid is subjected to an applied nominal stress, σ_n. The depth of the flaw and root radius of the flaw tip are denoted by a and ρ respectively. The flaw-tip hydrided region is represented by an infinitesimally thin process zone of length s. A uniform tensile stress, p_H is assumed in the process zone, while the relative displacement across the zone is denoted as $\delta(x)$.
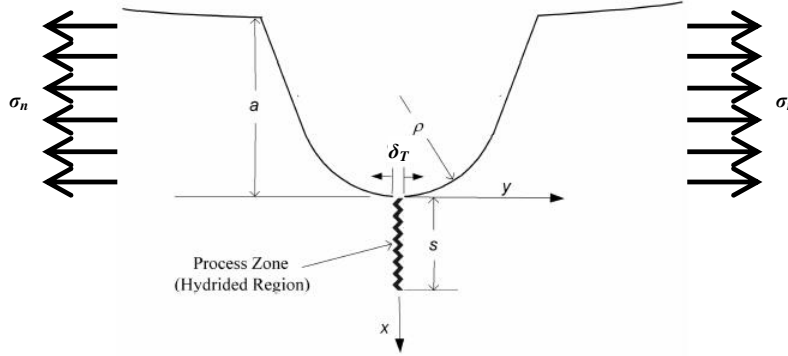

Figure 1 Model of a blunt flaw with associated process zone in semi-infinite solid.

The DHC initiation is deemed to occur when both the stress (p_H) and flaw root displacement ($\delta_T = \delta(x = 0)$) in the process zone reach some critical values, i.e., $p_H \geq p_c$ and $\delta_T \geq \delta_{Tc}$, where p_c and δ_{Tc} are treated as material properties and independent of the notch geometry. The DHC initiation criterion based on the simutaneous satisfactions of these two conditions takes into account for the stress relaxation due to hydride formation [26] as shown in Fig 2. The stress p_c is measured as the threshold stress for DHC initiation at a planar surface assuming the

formation of an "infinitely long" hydride. Specifically, for a long sharp crack at threshold condition such that $p_H = p_c$, the following relationship between p_c and δ_{Tc} is used.

$$\delta_{Tc} = \frac{K_{IH}^{2}}{E' p_c} \qquad (1)$$

where $E' = E$ for plane-stress condition and $E' = E/(1 - v^2)$ for plane-strain condition with E and v being Young's modulus and Poisson's ratio respectively; and K_{IH} is the isothermal threshold stress intensity factor associated with the onset of DHC growth from a long sharp crack.

As demonstrated in Fig 2, there exists a threshold peak flaw-tip stress σ_{pTH}. At the threshold condition, the process-zone restraining stress p_H decreases to p_c as δ_T increases from zero to δ_{Tc}. σ_{pTH} can be determined through analytical methods [7-9] (i.e., TPZ model) or numerical methods [10-12] (i.e., EPZ model).
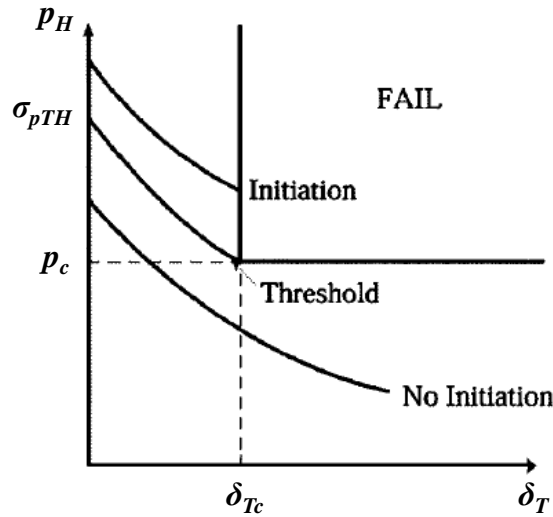

Figure 2 Schematic of stress relaxation representation in process-zone model [10, 11].

Smith [7-9] developed a general expression of σ_{pTH}/p_c that can cover a large variety of flaw configurations based on the "two extremes" method:

$$
\frac{\sigma_{pTH}}{p_c} =
\begin{cases}
1 + \kappa\psi & \text{, for small } \psi \quad (a) \\[2mm]
\mu\psi & \text{, for large } \psi \quad (b) \\[2mm]
1 + \dfrac{\psi(\kappa + \mu\psi)}{1+\psi} & \text{, for intermidiate } \psi \quad (c)
\end{cases}
$$

$$
\psi = \frac{K_{IH}}{p_c (\pi\rho)^{\frac{1}{2}}} \tag{d}
$$

$$ (2) $$

Under Mode I tension loading, the parameter κ in Eq. (2a) varies between 1.14 for a sharp flaw ($\rho/a = 0$), and 1.24 for a circular flaw ($\rho/a = 1$) [9]. The parameter μ in Eq. (2b) equals 2 for an elliptical flaw [9]. Equation (2c) is an interpolation function between Eqs. (2a) and (2b). Equation (2a) with $\kappa = 2$ is adopted in the literature [10, 11] wheres Smith [9] pointed out that using Eq. (2c) with $\kappa = 1.14$ and $\mu = 2$ leads to better prediction. Smith [9] further suggested using Eq. (2a) combined with the following κ parameter to construct the TPZ model for an intrusion type flaw:

$$
\kappa = 0.81\left[2\left\{1 + \left(\frac{2\rho}{a}\right)^{\frac{1}{2}}\right\}\right]^{\frac{1}{2}} \Big/ \left[1 + \frac{2}{3}\left(\frac{2\rho}{a}\right)^{\frac{1}{2}}\right]^{\frac{1}{2}} \tag{3}
$$

Figure 3(a) presents a comparison of the above-mentioned TPZ models proposed by Smith for 0.01 mm $\le \rho \le$ 0.5 mm. This range of root radius is of interest to DHC initiation in zirconium pressure tubes. Such a comparison has not been reported in the open literature according to our knowledge. The EPZ solution for a 45^0 V-shaped notch reported in [10] is also shown in Fig. 3(a). The plotted results are based on the experimental data reported in the literature [10], where $p_c = 450$ MPa, $K_{IH} = 7$ MPa$\sqrt{}$m and $a = 0.5$ mm. These parameters are also used in the remainder of this study to examine the σ_{pTH}/p_c - ρ relationship. Figure 3(a) suggests

that Eq. (2c) with $\kappa = 1.14$ and $\mu = 2$ agrees very well with the EPZ solution, while the predicted

σ_{pTH}/p_c from Eq. (2a) with $\kappa = 1.14$ to 1.24 and κ defined in Eq. (3) are slightly lower than the
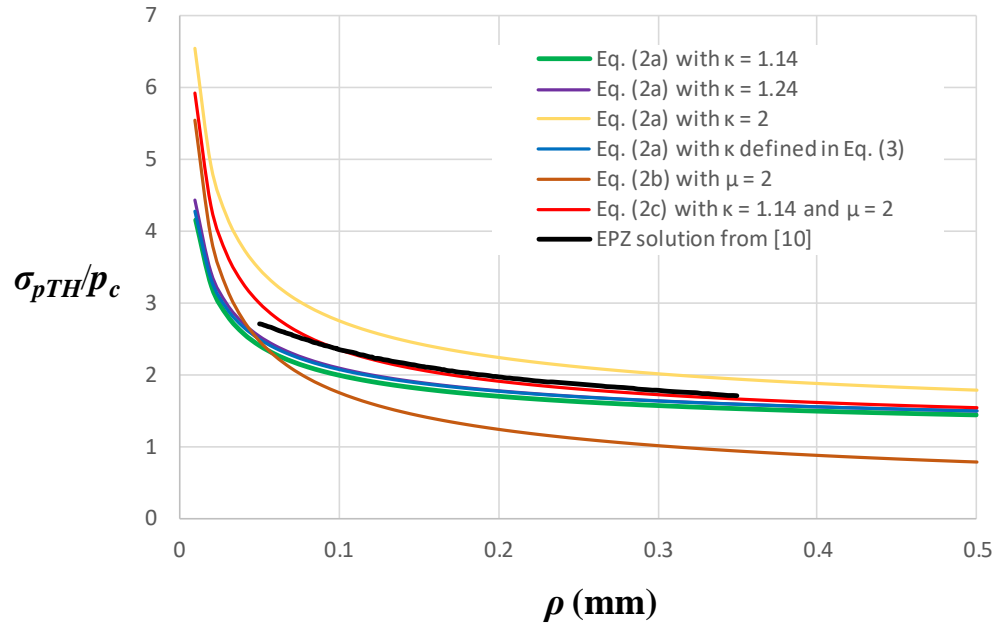
(a)
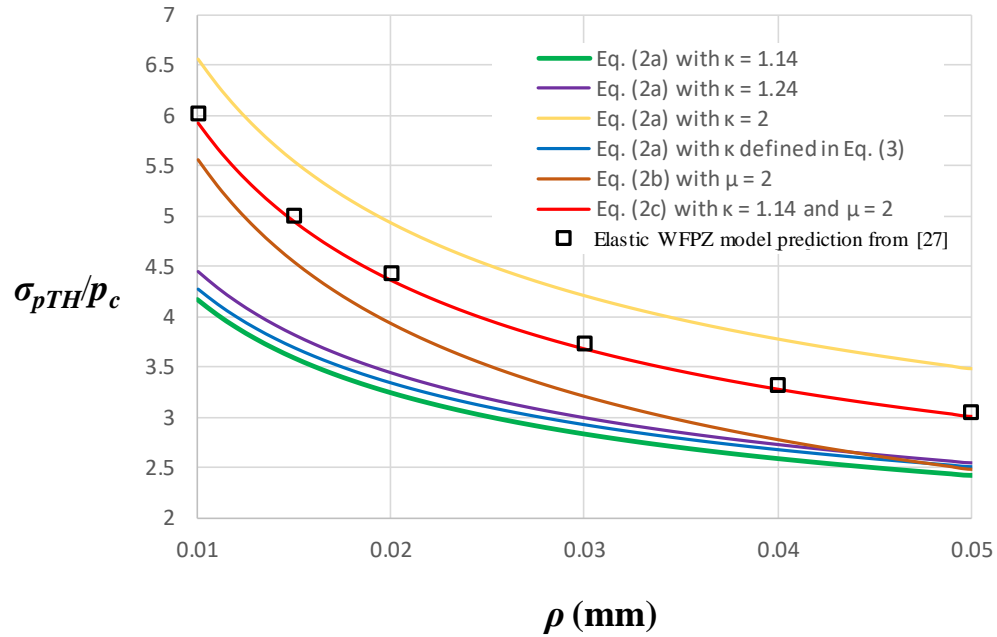
(b)

Figure 3 Variation of σ_{pTH}/p_c with ρ for different TPZ models proposed by Smith [9]; (a) 0.01 mm $\leq \rho \leq$ 0.5 mm, and (b) 0.01 mm $\leq \rho \leq$ 0.05 mm.

prediction from EPZ model. Compared with the EPZ solution, Eq. (2a) with $\kappa = 2$ consistently

overestimates σ_{pTH}/p_c as mentioned in [10], whereas Eq. (2b) with $\mu = 2$ underestimates it.

Figure 3(b) presents a comparison focusing on small root radii values, i.e., 0.01 mm $\leq \rho \leq$

0.05 mm. The prediction obtained from the elastic weight function-based process-zone (WFPZ)

model [27] is also shown in this figure. Note that the prediciton reported in [27] is in the form of

the threshold value of effective stress intensity factor (K_{TH}), and the relationship between K_{TH}

and σ_{pTH} is given in Section 4.2. Figure 3(b) indicates that for a small root radius, Eq. (2c) with

$\kappa = 1.14$ and $\mu = 2$ agrees well with the WFPZ solution. For the notch root radius $\rho = 0.01$ mm,

Eq. (2a) with $\kappa = 2$, Eq. (2b) with $\mu = 2$ and Eq. (2c) with $\kappa = 1.14$ and $\mu = 2$, lead to higher

values of σ_{pTH}/p_c, i.e. $5.5 \leq \sigma_{pTH}/p_c \leq 6.5$. On the other hand, the predicted σ_{pTH}/p_c from Eq. (2a)

with $\kappa = 1.14$ to 1.24 and κ defined in Eq. (3) is between 4.2 and 4.5. The values of σ_{pTH}/p_c from

these three solutions tend to converge to the solution from Eq. (2b) with $\mu = 2$ as ρ increases

from 0.01 mm to 0.05 mm.

3. TPZ Models for Blunt V-Notches

3.1 Near-tip stress field in sharp and blunt V-notches

A typical elastic stress field near the tip of a sharp V-notch (see Fig. 4(a)) under Mode-I

loading is expressed as:

$$
\left\{ \begin{array}{c} \sigma_{\theta\theta} \\ \sigma_{rr} \\ \tau_{r\theta} \end{array} \right\} = \frac{K_I^V}{\sqrt{2\pi}} r^{\lambda-1} \left\{ \begin{array}{c} f_{\theta\theta}\left(\theta,\beta,\lambda\right) \\ f_{rr}\left(\theta,\beta,\lambda\right) \\ f_{r\theta}\left(\theta,\beta,\lambda\right) \end{array} \right\} \tag{4}
$$

where K_I^V is a generalized sharp notch stress intensity factor (SN-SIF); r and θ are polar

coordinates with the origin at notch tip [Fig. 4(a)]; $\sigma_{\theta\theta}$, σ_{rr} and $\tau_{r\theta}$ are components of the stress

tensor; functions $f_{\theta\theta}(\cdot)$, $f_{rr}(\cdot)$ and $f_{r\theta}(\cdot)$ are reported in [28, 29]; β is half of the notch opening angle

as shown in Fig. 4(a); and the λ is the smallest real eigenvalue obtained from Eq. (5) given below [29].

$$\begin{cases} \sin(2\lambda\alpha) + \lambda\sin(2\alpha) = 0 \\ \alpha = \pi - \beta \end{cases} \tag{5}$$

For notch opening angle $0 \leq 2\beta \leq \pi$, Savruk and Kazberuk [22, 23] provided an empirical equation for λ as:

$$\lambda \approx 1 - \left(1.247\cos\beta - 1.312\cos^2\beta + 0.8532\cos^3\beta - 0.2882\cos^4\beta\right) \tag{6}$$
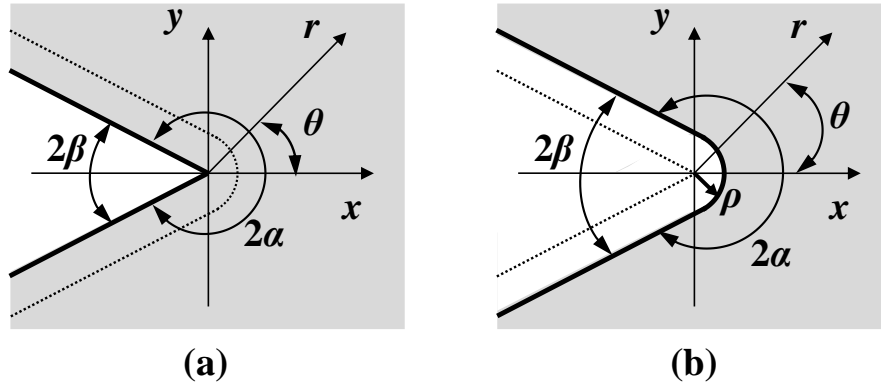

Figure 4 Schematics of the coordinate system near (a) Sharp and (b) blunt V-shaped notches.

Equation (6) is reported to have a absolute prediction error within 0.001. In the limit when $\beta = 0$ and $\lambda = 0.5$, Eq. (4) reduces to the well known crack tip stress field and K^V_I coincides with the stress intensity factor K_I defined in classical fracture mechanics.

For a V-Notch with blunt root (see Fig. 4(b)), the near-tip stress field is characterized by the blunt notch stress intensity factor (BN-SIF) $K^V_{\rho,I}$ [20, 21]:

$$\begin{Bmatrix} \sigma_{\theta\theta} \\ \sigma_{rr} \\ \tau_{r\theta} \end{Bmatrix} = \frac{K^V_{\rho,I}}{\sqrt{2\pi}} r^{\lambda-1} \begin{Bmatrix} g_{\theta\theta}(\theta,\beta,\lambda,\rho) \\ g_{rr}(\theta,\beta,\lambda,\rho) \\ g_{r\theta}(\theta,\beta,\lambda,\rho) \end{Bmatrix} \tag{7}$$

where $g_{\theta\theta}(\cdot)$, $g_{rr}(\cdot)$ and $g_{r\theta}(\cdot)$ are functions given in [20, 21]; and λ is determined from Eq. (5) and independent of ρ.

A stress rounding factor R_I can be used to relate SN-SIF and BN-SIF, i.e. $K^V_{\rho,I} = R_I K^V_I$, when ρ approaches zero. There have been a great deal of efforts in developing solutions of the R_I factor (e.g., Strandberg [19]; Filippi et al. [20]; Lazzarin and Filippi [21]; Savruk and Kazberuk [22, 23]; Savruk [24], Benthem [25] and Lazzarin and Tovo [30]). The main difference among these exisiting solutions is the different root tip profiles, e.g. circular, hyperbolic or curvilinear. Following solution given by Savruk and Kazberuk [22, 23] for a circular root is adopted in the present study.

$$\begin{cases} R_I = \dfrac{1+28.75\eta+98.04\eta^2-102.1\eta^3+47.42\eta^4-8.441\eta^5}{1+20.71\eta} \\ \eta = \dfrac{\pi}{2}-\beta \end{cases} \tag{8}$$

The notch-tip peak stress, σ_p, is related to $K^V_{\rho,I}$, and K^V_I through Eqs. (9) and (10) as:

$$\sigma_p = \frac{K^V_{\rho,I}}{\sqrt{2\pi}}\rho^{\lambda-1} = \frac{K^V_I}{\sqrt{2\pi}}\rho^{\lambda-1}R_I(\beta) \tag{9}$$

$$K^V_I = \lim_{\rho\to0}\frac{K^V_{\rho,I}}{R_I} = \frac{\sqrt{2\pi}}{R_I}\lim_{\rho\to0}\sigma_p\rho^{1-\lambda} \tag{10}$$

When the notch tip root radius $\rho = 0$, Eq. (7) reduces to Williams's solution [29], i.e. Eq. (4). σ_p can also be related to the remote nominal stress, σ_n, through the stress concentration factor (SCF), k_t, as,

$$\sigma_p = k_t\sigma_n \tag{11}$$

The SCFs for a large variety of specimens and flaw geometries are given in the literature (e.g. [16, 23]). To this end, the near-tip stress field can be determined if any of K^V_I, $K^V_{\rho,I}$, σ_p or k_t combined with σ_n is given for a specific loading and boundary condition.

3.2 Deformation fracture criterion for bodies with blunt V-shaped notches

Fracture initiation for elastic-plastic materials can be characterized by the deformation fracture criteria, which requires evaluation of plastic deformations near a flaw tip. Fracture initiation occurs when the plastic (or cohesive) zone reaches a critical length or when the notch tip opening displacement reaches a critical value [22, 23]. The well-known Dugdale–Bilby–Cottrell–Swinden (DBCS) plasticity band model [31, 32] is usually used in the analyses to establish the deformation fracture criteria. The model is based on assumption that plastic strain is confined to infinitesimally thin layers stemming from a crack tip [31, 32] or a blunt flaw [8, 22, 23]. The plasticity bands can be simulated as surfaces of displacement discontinuity at which cohesive stress are loaded, while materials outside the plasticity bands behave elastically. In such a way, the analysis is reduced to solving the boundary value problem within the realm of elasticity.
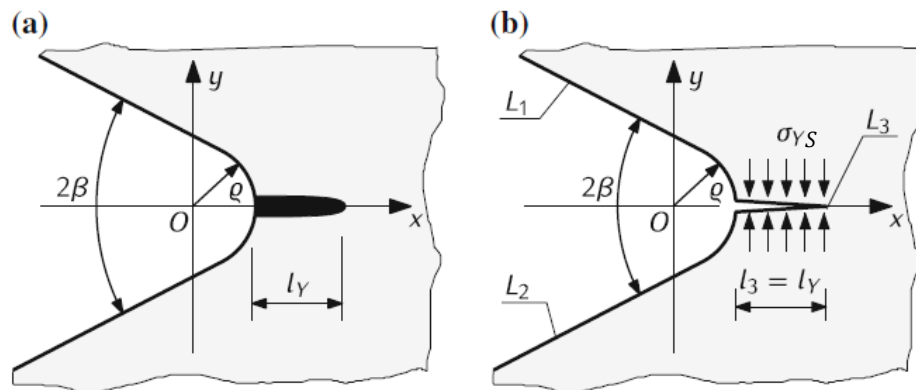

Figure 5 Schematics of the (a) plasticity band model and (b) fictitious crack representation for an infinite rounded V-shaped notch [23].

Figures 5(a) and 5(b) show the schematics of the plasticity band model for an infinite rounded V-shape notch. The plastic band is representd by a fictitious crack propagating from the tip of the notch (see Fig. 5(b)). Elastic-perfectly plastic materials is assumed in the plasticity band and therefore uniform cohesive stress equal to material yield strength (σ_{YS}) is loaded on the crack surface. The length of the plasticity band (l_Y) can be solved from the condition of zero stress intensity factor in the tip of the fictitious crack (K^{FC}_I):

$$K^{FC}_I\left(\gamma,\varepsilon,\beta\right)=K^{FC}_{\sigma_n}\left(K^V_I,\varepsilon,\beta\right)+K^{FC}_{\sigma_c}\left(\sigma_c,\varepsilon,\beta\right)=0 \qquad (12)$$

where σ_c denotes the uniform cohesive stress; $K^{FC}_{\sigma n}$ and $K^{FC}_{\sigma c}$ are the components of K^{FC}_I caused by the far-field nominal stress and cohesive stress, respectively. The dimensionless load, γ, and geometry parameter, ε, are given:

$$\begin{cases}\gamma=\dfrac{K^V_I}{\sigma_c\sqrt{2\pi}}\rho^{\lambda-1} & \text{(a)}\\[2em] \varepsilon=\dfrac{\rho}{l_Y} & \text{(b)}\end{cases} \qquad (13)$$

Similarly, the opening displacement at the notch tip (δ_T) can be calculated as the superposition of the components caused by the far-field nominal stress ($\delta_{T\sigma n}$) and cohesive stress ($\delta_{T\sigma c}$):

$$\delta_T\left(K^V_I,\gamma,\varepsilon,\beta\right)=\delta_{T\sigma_n}\left(K^V_I,\varepsilon,\beta\right)+\delta_{T\sigma_c}\left(\sigma_c,\varepsilon,\beta\right) \qquad (14)$$

Note that $K^{FC}_{\sigma n}$ and $\delta_{T\sigma n}$ are described by K^V_I that is induced by σ_n and without the presence of a fictitious crack. Crack initiation or propagation is considered when δ_T reaches a critical value, δ_{Tc}, which is a material property and related to σ_c following a cohesive separation law [33].

Define the dimensionless notch-tip opening displacement, $\tilde{\delta}_T$, as the following:

$$\tilde{\delta}_T=\dfrac{\delta_T E'\gamma^{\frac{\lambda}{\lambda-1}}}{\left(2\pi\right)^{\frac{1}{2}}K^V_I\rho^\lambda} \qquad (15)$$

Based on a complex variable method, Savruk and Kazberuk [23] calculated K^{FC}_I and δ_T in Eqs. (12) and (14) for the boundary value problem shown in Fig. 5(b), and determined $\tilde{\delta}_T$ by solving a singular integral equation consisting of kernel functions of displacement discontinuity in the plasticity band. Stable numerical results of $\tilde{\delta}_T$ corresponding to $\pi/36 \le 2\beta \le 130\pi/180$ and $0.3365 \le \gamma \le 10$ are obtained and shown in Fig. 6 [23].
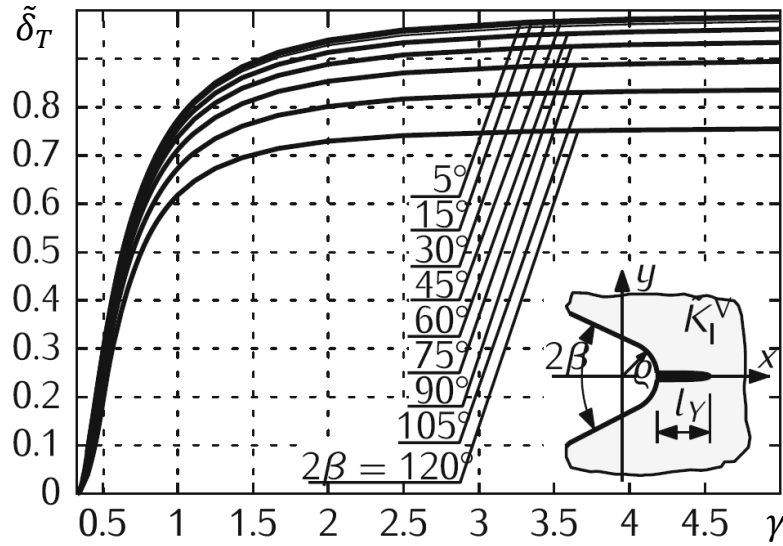

Figure 6 Numerical results of $\tilde{\delta}_T$ by Savruk and Kazberuk [23].

3.3 TPZ model based on Savruk and Kazberuk's solution

The process-zone models for DHC initiation reported in [8, 10, 27] were developed based on the same plasticity bands model as described in the previous section, while the uniform cohesive stress is set equal to the cohesive strength of the process zone, i.e. $\sigma_c = p_c$ ($p_c < \sigma_{YS}$). For TPZ models in [8], Eqs. (12) and (14) were solved by using complex variable and conformal mapping methods. While for EPZ models [10, 27], these equations were solved with the aid of finite element analyses or parametric solutions for stress field. The cohesive separation law for the process zone is given as:

$$G_c = \frac{K_{IH}^2}{E'} = \delta_{Tc} p_c \qquad (16)$$

where G_c is the work of separation. Note that Eq. (16) is consistent with Eq. (1).

In this paper, the solution of $\tilde{\delta}_T$ obtained by Savruk and Kazberuk [23] is used to construct the TPZ model. Based on the condition $\sigma_c = p_c$ and Eq. (13a), Eq. (15) is rearranged as:

$$\begin{cases} \delta_T = \dfrac{\pi \rho\, p_c}{E'} \tilde{Q}(\lambda, \gamma) & \text{(a)} \\[2mm] \tilde{Q}(\lambda, \gamma) = 2\tilde{\delta}_T \gamma^{\frac{1}{1-\lambda}} & \text{(b)} \end{cases} \qquad (17)$$

For practical applications, parameter $\tilde{Q}$ is expressed as a cubic function of $(\gamma - 1/R_I)$

$$\tilde{Q}(\lambda, \gamma) = \sum_{k=1}^{3} Q_k \left(\gamma - \frac{1}{R_I} \right)^k \qquad (18)$$

where Q_k ($k = 1$, 2 or 3) are the coefficients of the cubic expansion based on the least square regression of the curves shown in Fig. 6.

Table 1 lists Q_1, Q_2 and Q_3 for different β values. The curve fitting accuracy corresponds to $R^2 \geq 0.9999$. It is found that $\tilde{\delta}_T$ is not sensitive to β when $2\beta \leq 45°$, therefore the coefficients Q_k for $2\beta = 45°$ in Table 1 also apply to $2\beta \leq 45°$.

Table 1 Coefficients Q_k in Eq. (18) and Q^* in Eq. (24).

2β	45°	60°	75°	90°	105°	120°
λ	0.5049	0.5120	0.5246	0.5446	0.5742	0.6159
R_I	2.9997	2.9870	2.9577	2.9024	2.8085	2.6603
Q_1	0.8244	0.7747	0.6851	0.568	0.3113	0.0854
Q_2	2.2118	2.2485	2.3131	2.387	2.5579	2.5958
Q_3	-0.0289	-0.0058	0.016	0.0686	0.1657	0.4434
Q^*	2.1247	2.2329	2.3411	\	\	\

Based on Eqs. (9) and (13a), γ can be related to σ_p as,

$$\gamma = \frac{K_I^V}{p_c\sqrt{2\pi}}\rho^{\lambda-1} = \frac{\sigma_p}{p_c R_I} \tag{19}$$

Combining Eqs. (17) - (19), the DHC initiation is triggered when $\delta_T = \delta_{Tc}$ and γ reaches a threshold value, γ_{TH} defined by:

$$\begin{cases} \delta_{Tc} = \dfrac{\pi\rho p_c}{E'}\displaystyle\sum_{k=1}^{3} Q_k\left(\gamma_{TH}-\dfrac{1}{R_I}\right)^k & \text{(a)} \\[3mm] \gamma_{TH} = \dfrac{\sigma_{pTH}}{p_c R_I} & \text{(b)} \end{cases} \tag{20}$$

The DHC initiation also requires $\sigma_{pTH}/p_c \geq 1$ and therefore $\gamma_{TH} \geq 1/R_I$. Invoking Eqs. (1), (2d) and (20a), (γ_{TH} - $1/R_I$) can be solved as the real root of the following cubic function.

$$\sum_{k=1}^{3} Q_k\left(\gamma_{TH}-\frac{1}{R_I}\right)^k = \psi^2 \tag{21}$$

σ_{pTH}/p_c can be expressed as:

$$\frac{\sigma_{pTH}}{p_c} = \begin{cases} 1+R_I\left[-\dfrac{Q_2}{3Q_3}+2\sqrt{-\omega}\cos\left[\dfrac{\arccos\dfrac{\chi}{(-\omega)^{\frac{3}{2}}}}{3}\right]\right] & \text{,if } Q_3 > 0 \\[6mm] 1+R_I\left[-\dfrac{Q_2}{3Q_3}+2\sqrt{-\omega}\cos\left[\dfrac{\arccos\dfrac{\chi}{(-\omega)^{\frac{3}{2}}}-2\pi}{3}\right]\right] & \text{,if } Q_3 < 0 \end{cases} \tag{22}$$

where

$$\begin{cases} \chi = -\dfrac{Q_2^{\,3}}{27Q_3^{\,3}}+\dfrac{Q_1 Q_2}{6Q_3^{\,2}}+\dfrac{\psi}{2Q_3} \\[4mm] \omega = -\dfrac{Q_2^{\,2}}{9Q_3^{\,2}}+\dfrac{Q_1}{3Q_3} \end{cases} \tag{23}$$

For simplicity, if $2\beta \leq 75°$, Eq. (18) can be reduced to a quadratic function of γ with similar fitting accuracy:

$$\hat{Q}(\lambda,\gamma) = Q^* \gamma \left(\gamma - \frac{1}{R_I} \right) \tag{24}$$

where the fitting coefficient Q^* is given in Table 1.

Accordingly, σ_{pTH}/p_c is given as,

$$\frac{\sigma_{pTH}}{p_c} = \frac{1}{2}\left[1 + \sqrt{1 + \frac{(2R_I\psi)^2}{Q^*}} \right] \tag{25}$$

Figure 7(a) shows the values of σ_{pTH}/p_c obtained from Eq. (22) for $90° \leq 2\beta \leq 120°$ and Eq. (25) for $2\beta \leq 75°$ corresponding to 0.01 mm $\leq \rho \leq$ 0.5 mm. Equation (2c) with $\kappa = 1.14$ and $\mu = 2$ as well as the EPZ solution [10] are also shown for comparison. A zoomed-in view of this figure in the range 0.01 mm $\leq \rho \leq$ 0.05 mm is shown in Fig. 7(b). It is observed from Fig. 7(a) that the proposed TPZ solution has a minor dependence on the β values when $\rho \geq 0.1$ mm. On the other hand, as observed in Fig. 7(b), the opening angle has a relatively large influence on the predicted σ_{pTH}/p_c for small root radii. For example, when $\rho = 0.02$ mm, the predicted σ_{pTH}/p_c for $2\beta \leq 45°$ is 16% higher than the solution corresponding to $2\beta = 120°$. Figures 7(a) and 7(b) also indicate that the proposed TPZ solution agrees well with the EPZ solutions. These figures suggest that Eq. (2c) with $\kappa = 1.14$ and $\mu = 2$ is in general consistent with the proposed TPZ solution with $75° \leq 2\beta \leq 105°$ when 0.01 mm $\leq \rho \leq$ 0.5 mm. The new results of Eqs. (22) and (25) are more advantageous than the theoretical model of Eq. (2c) with fixed values of μ and κ because the current model takes into acount for the influence of the opening angle of a V-shaped notch.
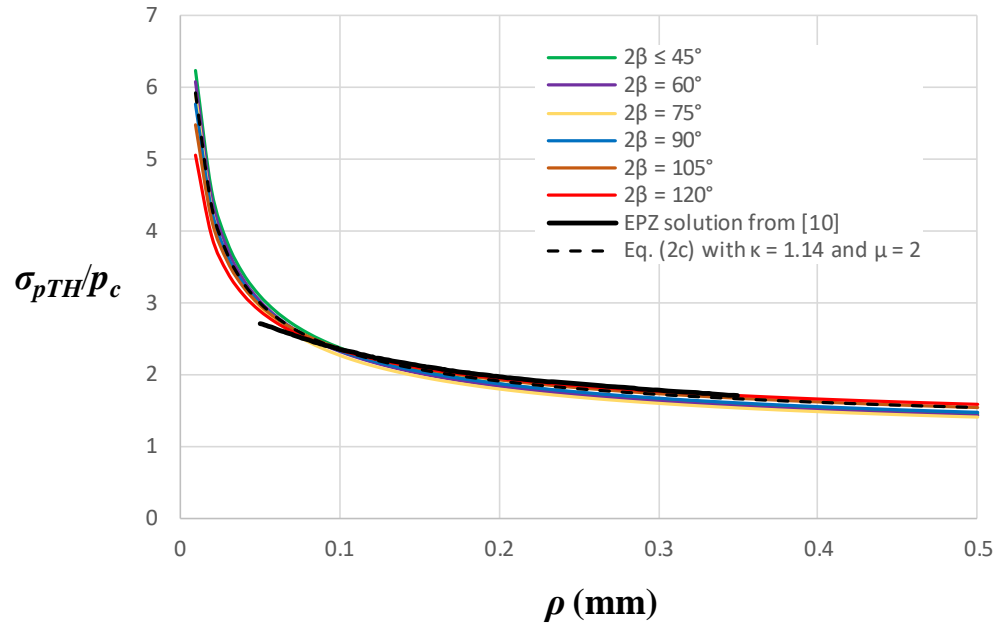
(a)
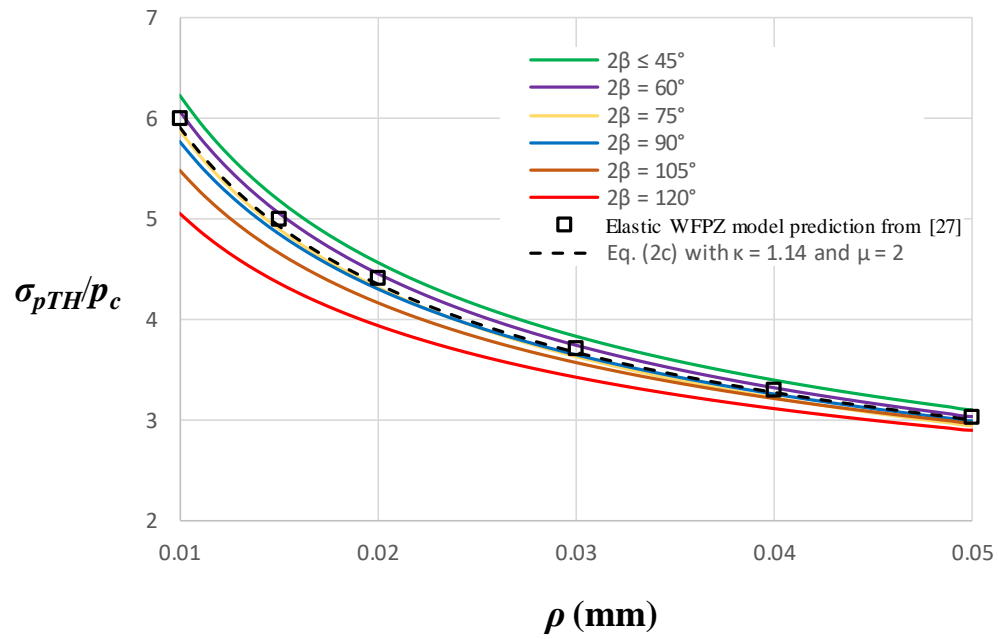
(b)

Figure 7 Proposed TPZ model based on Savruk and Kazberuk's solution [23] corresponding to (a) 0.01 mm $\leq \rho \leq$ 0.5 mm, and (b) 0.01 mm $\leq \rho \leq$ 0.05 mm.

4. Experimental Verification of the Proposed TPZ Model

4.1 V-notched specimens with root radius larger than 0.05 mm

The results from DHC initiation tests on two groups of small notched cantilever beam specimens with notch opening angle $2\beta = 45°$ reported in Ref. [27] are used to verify the proposed theoretical process-zone model. Specimens from Group I were cut from the ex-service, pre-irradiated pressure tube [34] while the Group II specimens were made by un-irradiated pressure tube materials [34]. Table 2 lists the mean and lower-bound values of K_{IH} and yield strength, σ_{YS} for these materials. The cohesive strength in the process zone model, p_c, is set to be 450 MPa for these predictions. All specimens were loaded to a specified outer-fiber bending stress at room temperature and then held at a certain temperature to simulate flaw-tip stress relaxation due to creep under normal operating conditions. After the creep cycle, the specimens were subjected to hydride ratcheting thermal cycles that simulated reactor heat-up/cool-down cycles under a specified constant loading. For specimens with root radii larger than 0.05 mm, the maximum (peak) temperature of the entire thermal cycle is 275°C and the duration of the creep cycle is 120 hours. A total of 22 out of the 176 specimens in Group I and 13 out of 65 specimens in Group II failed.

Figures 8(a) and 8(b) show the DHC initiation experimental data of threshold peak flaw-tip stress σ_{pTH} for specimens in Groups I and II, respectively. For comparision, the predicted σ_{pTH} obtained from Eq. (25) as well as the EPZ solutions [10, 11] incorporating the elastic FEA are shown. All specimens had 45° V-notches with 0.06 mm $\leq \rho \leq$ 0.32 mm and 0.1 mm $\leq a \leq$ 1.1 mm for Group I test, and 0.1 mm $\leq \rho \leq$ 0.5 mm and 0.5 mm $\leq a \leq$ 1.2 mm for Group II test. The predictions in these figures were based on the notch depth $a = 0.5$ mm. It is observed from Fig. 8(a) that Eq. (25) as well as the elastic EPZ model give reasonable agreement with the experimental results. As shown in Fig. 8(b), the proposed TPZ model and the EPZ model in Ref.

[11] lead to very similar and conservative predictions for $\rho > 0.1$ mm. For $\rho = 0.1$ mm, Eq. (25) based on mean K_{IH} leads to a higher and less conservative prediction than the elastic EPZ solution according to the Group II test data of failed samples.

Table 2 Material property and C_δ factors for the process-zone model.

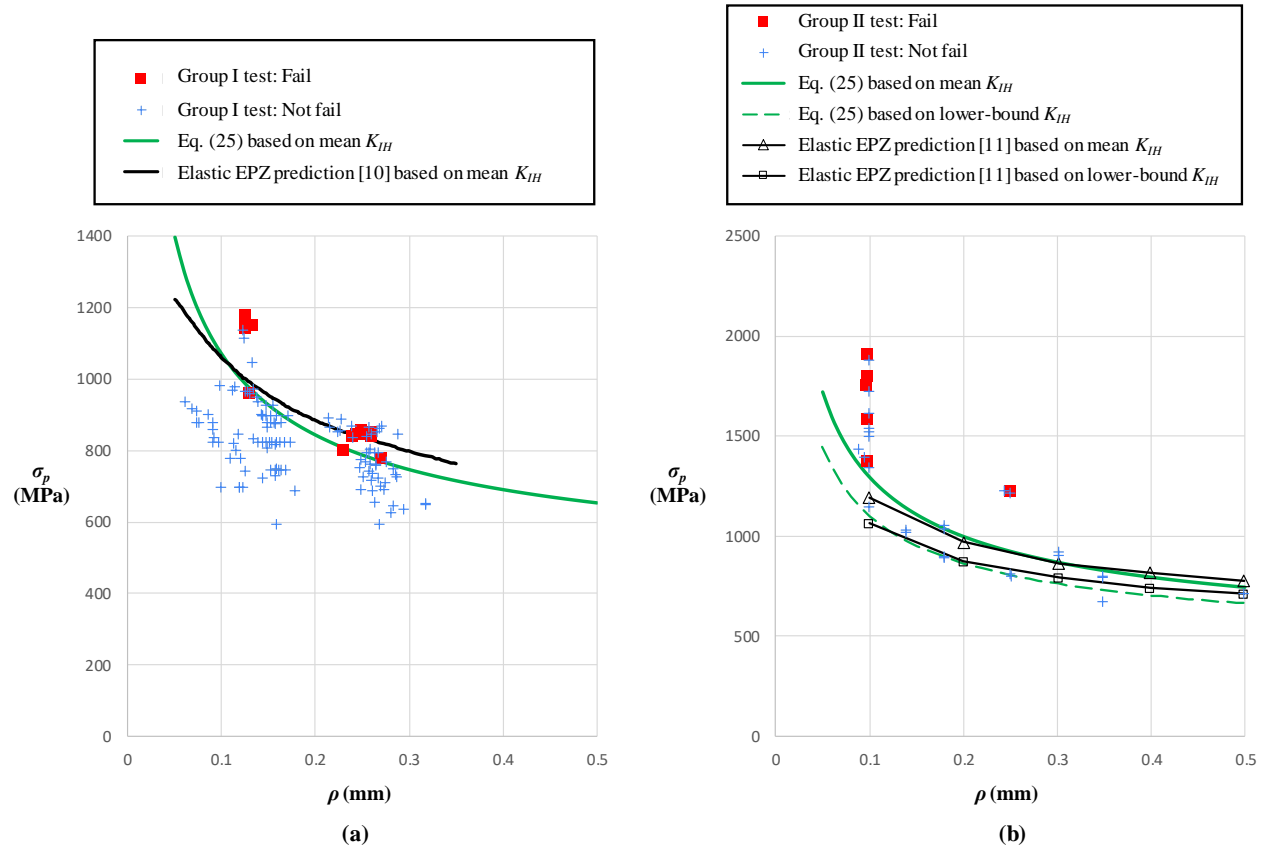|	Mean K_{IH} (MPa√m)	Lower-bound K_{IH} (MPa√m)	Peak Temperature of the entire thermal cycle (°C)	σ_{YS} (MPa)	C_δ in Eq. (31) for $\rho = 0.015$ mm					
					ξ					
					0	0.08	0.16	0.24	0.32	0.4
Group I (Irradiated material)	7.0	6.4	275	749	1.000	1.170	1.340	1.510	1.680	1.850
			300	720	1.000	1.197	1.393	1.590	1.786	1.983
Group II (Un-Irradiated material)	9.0	7.3	275	582	1.000	1.219	1.437	1.656	1.875	2.094
			300	571	1.000	1.248	1.496	1.744	1.992	2.239

Figure 8 Elastic process-zone prediction and experimental results of σ_{pTH} corresponding to (a) Group I, and (b) Group II specimens with $\rho \geq 0.05$ mm (Experimental results were digitized from

4.2 V-notched specimens with root radius smaller than 0.05 mm

The test specimens with notch root radii smaller than 0.05 mm in Group I and Group II were subjected to a pre-hold under load at 300°C for 1000 hours (120 hours for Group II) to induce notch-tip stress relaxation due to creep, followed by hydride ratcheting thermal cycles with a peak temperature of 270°C. A total of 6 out of the 32 specimens in Group I and 16 out of 42 specimens in Group II failed.

For specimens with root radii smaller than 0.05 mm, the peak stress is very high and therefore not a practical measure of the threshold conditions for DHC initiation [1]. For such small root radii, it is more convenient to characterize the loading level in terms of the effective SIF [1, 15, 27], K_{eff}, as calculated for a crack with the same planar dimension as the notch. Note that,

$$K_{eff} = \frac{\sigma_p}{k_t}\sqrt{\pi a}F\left(\frac{a}{W}\right) \tag{26}$$

where $W = 4.2$ mm [15] is the specimen thickness (tube wall thickness), and the function $F(a/W)$ for a pure bending single-edge notched specimen is given by Tada et al. [35] as:

$$F\left(\frac{a}{W}\right) = 1.122 - 1.4\left(\frac{a}{W}\right) + 7.33\left(\frac{a}{W}\right)^2 - 13.08\left(\frac{a}{W}\right)^3 + 14\left(\frac{a}{W}\right)^4 \tag{27}$$

Stress concentration factor k_t for the arc cantilever beam (with geometry given in [14]) under bending loading are evaluated from two-dimensional elastic FEA using the computer code ANSYS [36] and listed in Table 3.

The threshold value of K_{eff}, K_{TH}, can be evaluated from Eq. (26) based on the given σ_{pTH}. Similarly, σ_{pTH} can be backcalculated from the given K_{TH}. In this way, the σ_{pTH} for very small root radii corresponding to the WFPZ model [27] are calculated as shown in Figs. 3(b) and 7(b).

Table 3 Values of k_t in Eq. (26).

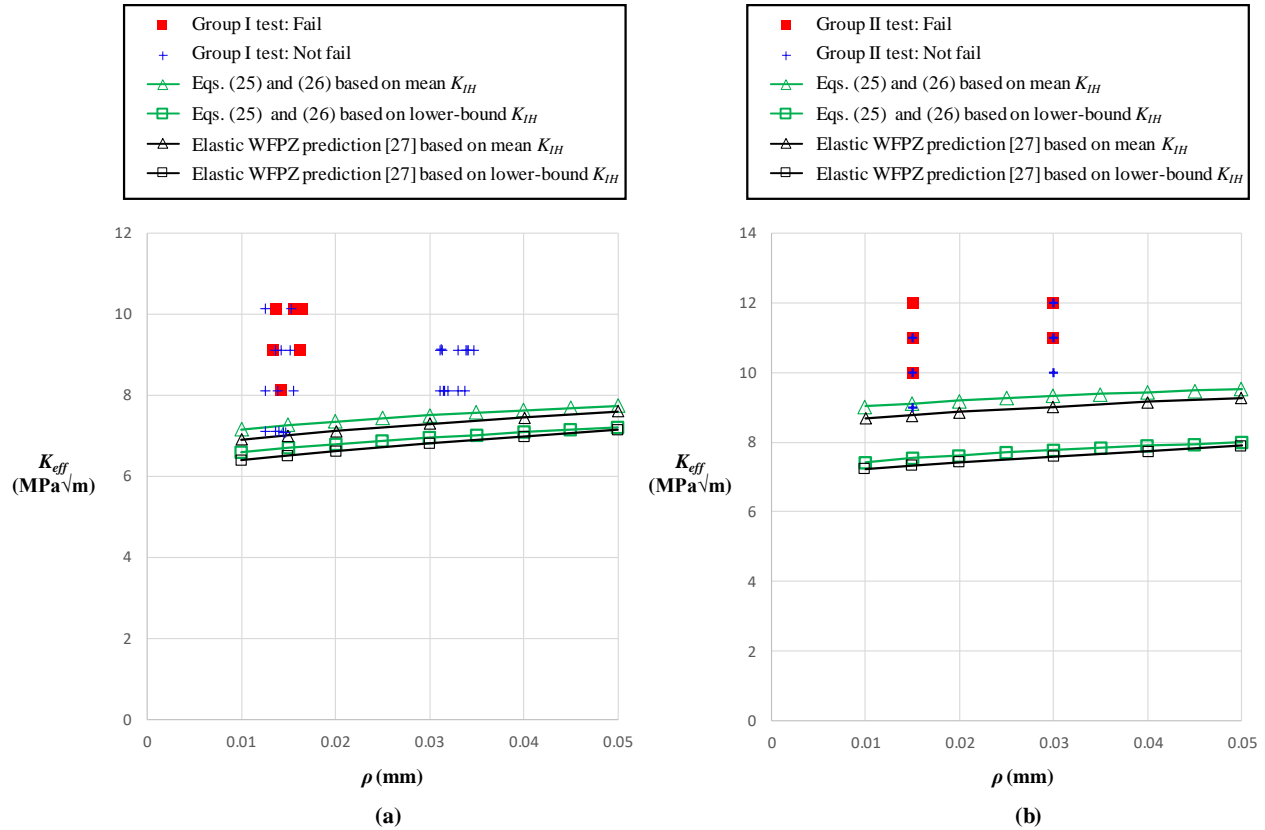| ρ (mm)	k_t
0.01	19.894
0.015	16.326
0.02	14.197
0.025	12.745
0.03	11.673
0.035	10.846
0.04	10.172
0.045	9.624
0.05	9.150

Figure 9 Elastic process-zone prediction and experimental results of K_{TH} corresponding to (a) Group I, and (b) Group II specimens with $\rho \leq 0.05$ mm (Experimental results were digitized from Ref. [27]).

Figures 9(a) and 9(b) show the DHC initiation experimental data, the proposed elastic

TPZ and elastic WFPZ [27] predictions of K_{TH} for irradiated specimens with $a = 0.75$ mm and $0.01 \leq \rho \leq 0.05$ mm. These figures indicate that although both the proposed TPZ model and the elastic WFPZ model consistently underestimate the test data of K_{TH}, the proposed TPZ model yields slightly less conservative predictions compared to the WFPZ model.

4.3 Impact of Plasticity and Flaw Tip Constraint

Aforementioned TPZ and EPZ solutions are based on the assumption that DHC initiation occurs under elastic loading conditions. To satify this requirement, p_c must be less than the material yield strength, σ_{YS}, and the root radius ρ should be sufficiently large. In the case when ρ is small, plastic deformations occur at the root of the flaw prior to hydride formation [1]. Recall that the process zone is represented by an infinitesimally thin hydride layer, the process-zone displacement (δ), measured as the expansion of the thickness of the hydride region, is considered totally contributing to DHC initiation [1]. The flaw-tip plasticity prior to hydride formation has an impact on the magnitude of δ_T. To analytically account for stress relaxation by plastic deformation and the constraint effects, Scarth and Smith [11] introduce an additional process zone with the uniform tensile stress (σ_{yc}) that is both greater than p_c and σ_{YS}. The elastic-plastic flaw-tip opening displacement $\delta_T(ep)$ is then calculated as [1],

$$\delta_T \left(ep \right) = \delta_T \left(e \right) - \delta_y \qquad (28)$$

where $\delta_T(e)$ is the elastic flaw-tip opening displacement and determined through Eq. (14); and δ_y is the opening displacement corresponding to the additional process zone that accounts for the effect of prior plastic relaxation.
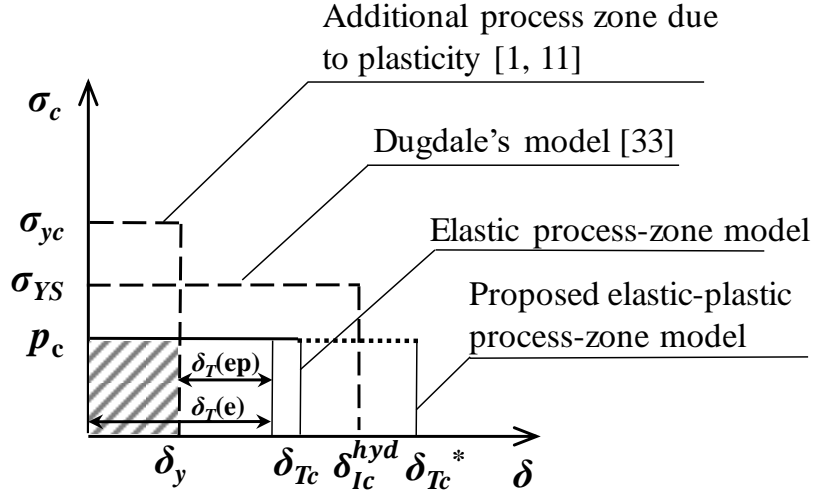
Figure 10 Separation laws for the process zone models

It was found that both the elastic-plastic threshold applied nominal stress, σ_{nTH}, and K_{TH} are underestimated through the use of elastic TPZ and EPZ models [1, 11]. In the sample calculation reported in [1, 11], when $p_H = p_c$ in the hydride process zone, DHC initiation is considered to occur assuming flaw tip elastic behavior since $\delta_T(e)$ already exceeds δ_{Tc}, whereas no DHC initiation is predicted when plasticity is taken into account as $\delta_T(ep) < \delta_{Tc}$. Figure 10 demonstrates different separation laws associated with the elastic-plastic process-zone models. For certain separation law, the work of separation, G_c, is described by the area under the $\sigma_c - \delta$ curve [33]. The correction provided by Eq. (28) is considered as an approximation to show the plasticity effect [1] while it is not clear how to obtain reliable values of σ_{yc} and δ_y. Using Dugdale's model (see Fig. 10) to simulate both plasticity and hydride region can be another option as the following separation law is well accepted:

$$G_{Ic}^{hyd} = \frac{\left(K_{Ic}^{hyd}\right)^2}{E'} = \delta_{Ic}^{hyd}\sigma_{YS} \tag{29}$$

where G^{hyd}_{Ic}, K^{hyd}_{Ic} and δ^{hyd}_{Ic} are the critical energy release rate, fracture toughness and critical crack tip opening displacement for hydrided materials, respectively.

However, the experimental data of K^{hyd}_{Ic} is very limited. Using K_{IH} rather than K^{hyd}_{Ic} to

build up the process-zone separation law is more practical because the former is reliably obtained based on a large number of different ex-service pressure tubes under a range of service conditions [1]. In fact, if materials hardening behavior as well flaw tip constraint needs to be considered, the actual cohesive law is much more complicated and hardly characterized by the uniform cohesive stress representation. In this paper, a simple elastic-plastic cohesive model is proposed that can potentially reduce the conservatism caused by the flaw-tip plasticity and constraint effect.

Assume a new process zone with a cohesive strength equal to p_c but a higher critical notch-tip opening displacement, $\delta_{Tc}^* = C_\delta \delta_{Tc}$ and $C_\delta \geq 1$ (see Fig. 10). The proposed model can be interpreted from the view of energy, more external work is required to drive the DHC initiation because part of the energy will be dissipated due to flaw-tip plasticity. The values of G_c, K_{IH} and ψ for this new process zone are denoted as G_c^*, K_{IH}^* and ψ^* and defined as,

$$
\begin{cases}
G_c^* = C_\delta G_c & \text{(a)} \\
K_{IH}^* = K_{IH}\sqrt{C_\delta} & \text{(b)} \\
\psi^* = \dfrac{K_{IH}^*}{p_c\left(\rho\pi\right)^{\frac{1}{2}}} = \psi\sqrt{C_\delta} & \text{(c)}
\end{cases}
\tag{30}
$$

The proposed elastic-plastic TPZ solution is characterized by Equation (25) with ψ being replaced by ψ^* determined from Eq. (30c). The following empirical expression of C_δ is proposed to account for both plasticity and constraint effect on the process-zone model.

$$
C_\delta = 1 + \xi \frac{p_c}{\sigma_{YS}} \ln\left(1 + \frac{a}{\rho}\right)
\tag{31}
$$

where ξ ($\xi \geq 0$) is an empirical factor depending on the level of conservatism.

Equation (31) is proposed in a similar logarithmic form that expressing the maximum normal stress in the plastic zone ahead of the notch [14], while the terms a/ρ and p_c/σ_{YS} are also

similar to the ones used in Ref. [27]. It is clear that C_δ increases as a/ρ or p_c/σ_{YS} increases, corresponding to a higher constraint level. For specimen without a flaw/crack, i.e. $a/\rho = 0$, $C_\delta = 1$. The proposed C_δ defined by Eq. (31) also accounts for the temperature effects on the prediction because σ_{YS} is temperature-dependent. Figure 11 shows the C_δ - ρ relations for $\xi = 0$ to 0.4 associated with Group I specimens with $\sigma_{YS} = 749$ MPa and $a = 0.5$ mm. The figure suggests that C_δ increases with increasing ξ and decreasing ρ, as expected. The C_δ values corresponding to $\rho = 0.015$ mm are between 1 and 1.85. Table 2 lists the values of C_δ corresponding to $\rho = 0.015$ mm and $\xi = 0$ to 0.4 for Group I and Group II specimens. Note that when $\xi = 0$, the elastic-plastic TPZ model will be reduced to the elastic one.
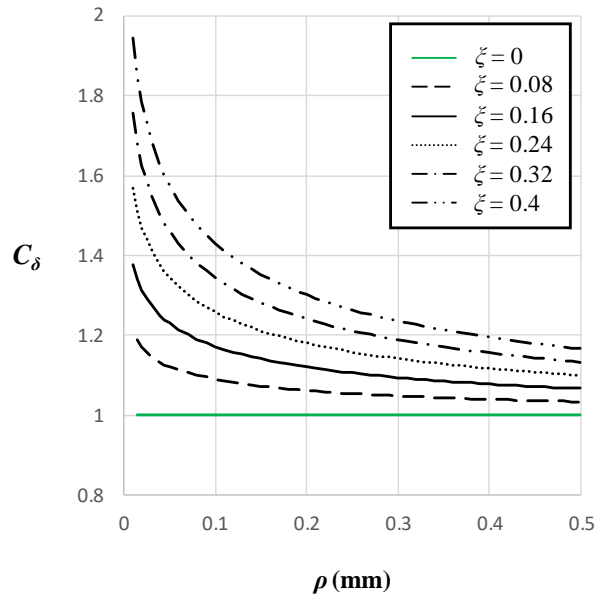

Figure 11 Values of C_δ for Group I specimens with $\sigma_{YS} = 749$ MPa and $a = 0.5$ mm.

Figures 12 and 13 compare the predicted σ_{pTH} and K_{TH} based on the proposed elastic-plastic TPZ model and the proposed C_δ determined from Eq. (31). All the predictions are based on the lower-bound K_{IH} values as listed in Table 1. For specimens with notch root radius higher than 0.05 mm, notch depth $a = 0.5$ mm is considered. Figures 12 and 13 suggest that using the proposed elastic-plastic TPZ model in general achieve an improvement of DHC prediction. The

predicted $\sigma_{pTH}(K_{TH})$ - ρ relation from the proposed elastic-plastic TPZ model tends to shift up and therefore reduce the conservatism when $\xi \leq 0.16$. For example, the prediction errors associated with the lowest K_{TH} corresponding to $\rho = 0.015$ mm in Figs. 13(a) and 13(b) are about 17% and 25% if elastic TPZ model (i.e. $\xi = 0$) is adopted. These errors are reduced to 4% and 10% if elastic-plastic TPZ model with $\xi = 0.16$ is used in the prediction. On the other hand, elastic-plastic TPZ model with $\xi \geq 0.24$ may lead to nonconservative prediction. Based on a trial and error procedure on the available test results, $\xi = 0.2$ can lead to optimized predictions corresponding to Eq. (25). It must be noted that the proposed approach for developing the elastic-plastic TPZ solution is based on limited number of experimental results, and must be further validated before being applied to the evaluation of in-service flaws in pressure tubes.
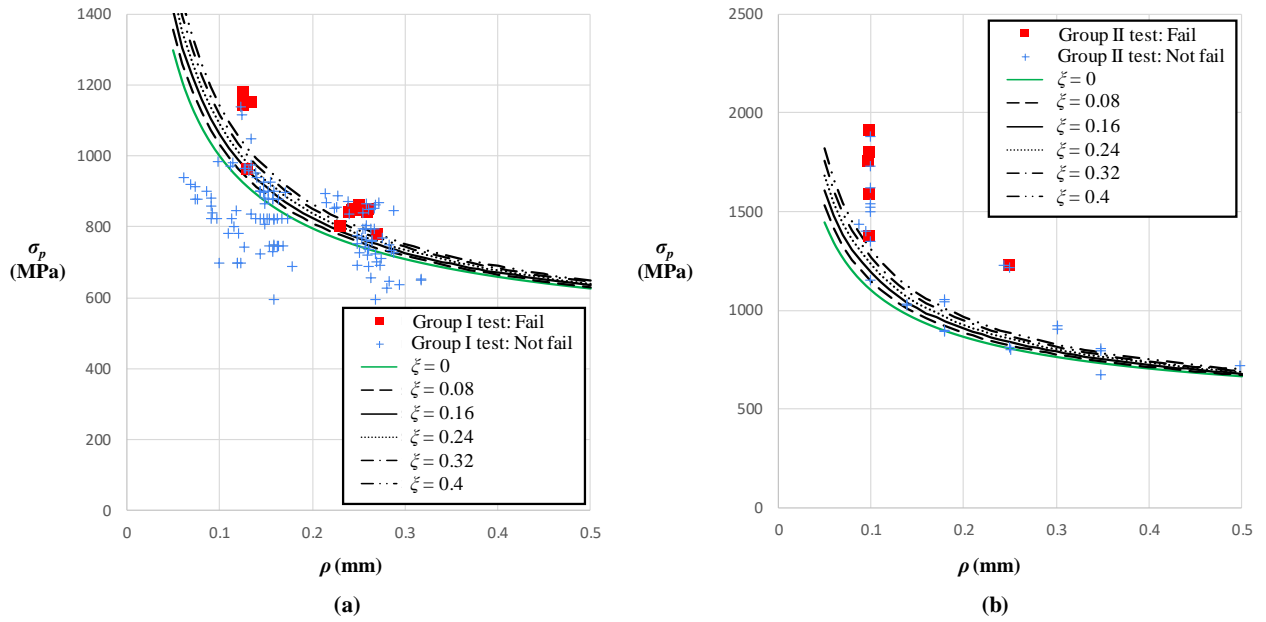

Figure 12 Elastic-plastic TPZ predictions based on lower-bound K_{IH} and experimental results of σ_{pTH} corresponding to (a) Group I, and (b) Group II specimens with $\rho \geq 0.05$ mm (Experimental results were digitized from Ref. [27]).
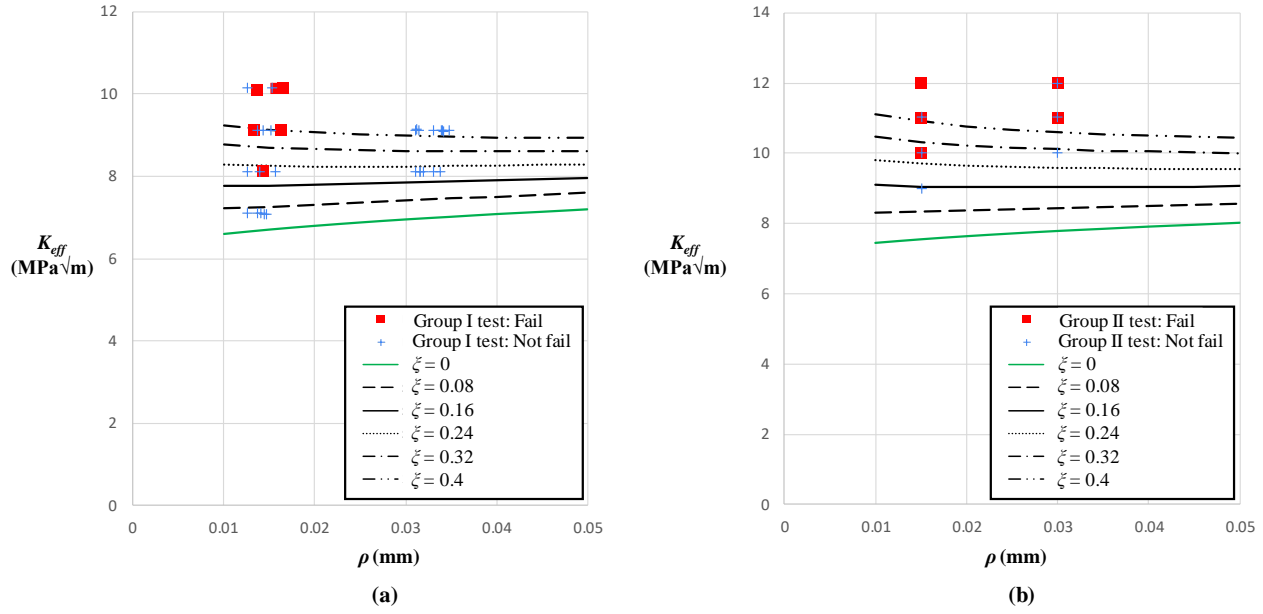
Figure 13 Elastic-plastic TPZ predictions based on lower-bound K_{IH} and experimental results of K_{TH} corresponding to (a) Group I, and (b) Group II specimens with $\rho \leq 0.05$ mm (Experimental results were digitized from Ref. [27]) .

5. Conclusions

The key findings and conclusions of the present study are summarized below.

1) Several TPZ models for semi-elliptical or intrusion type flaws proposed by Smith are reviewed and compared with the EPZ solution for a 45^0 V-shaped blunt notch. It is found that Eq. (2c) with $\kappa = 1.14$ and $\mu = 2$ agrees very well with the EPZ solution, while the σ_{pTH}/p_c values predicted from Eq. (2a) with $\kappa = 1.14$ to 1.24 and κ defined by Eq. (3) are slightly lower than the prediction from the EPZ model. Compared to the EPZ solution, Eq. (2a) with $\kappa = 2$ results in consistent over estimations, whereas Eq. (2b) with $\mu = 2$ leads to underestimations.

2) Making use of the analytical solutions and deformation fracture criteria for blunt V-notches proposed by Savruk and Kazberuk, an improved TPZ model is developed that also considers the effect of notch angle. Comparisons with experimental data show that the new model based on Savruk and Seweryn solution has a similar prediction accuracy compared to the EPZ and WFPZ solutions but does not require iterations and FEA or the use of prametric

solutions for the notch tip stress field.

3) An empirical C_δ factor that depends on the ratios of process zone strength to yield strength (p_c/σ_{YS}) and flaw depth to notch root radius (a/ρ) and an empirical constant ξ determined through trial and error, is proposed to account for plasticity and constraint effects. It is shown that the modified TPZ model with C_δ presents a further improvement of DHC prediction. However, this model requires further validation with extensive experimental results.

The proposed models can facilitate the design and integrity assessment of nuclear reactor pressure tubes through a computationally efficient procedure that also reduce conservatism in predictions.

Acknowledgments

References

[1] Puls, M.P. (2012). The effect of hydrogen and hydrides on the integrity of zirconium alloy components: delayed hydride cracking. Springer Science and Business Media.

[2] Simpson, C.J. and Ells, C.E. (1974), Delayed hydrogen embrittlement of Zr-2.5 wt % Nb, *Journal of Nuclear Materials*, 52, 289–295.

[3] Dutton, R., Nuttall, K., Puls, M.P., and Simpson, L. A., (1977), Mechanisms of hydrogen induced delayed cracking in hydride forming materials, *Metallurgical and Materials Transactions A*, 10(8), 1553–1562.

[4] Smith, E. (1995). The initiation of delayed hydride cracking at a blunt flaw. *International journal of pressure vessels and piping*, 62, 9–17.

[5] Simpson, L.A., Puls, M.P. (1979). The effects of stress, temperature and hydrogen content on hydride-induced crack growth in Zr-2.5 pct Nb. *Metallurgical and Materials Transactions A*, 10(8), 1093–1105.

[6] Anon. (1996) Technical Basis for the Fitness-for-service Guidelines for Zirconium Alloy Pressure Tubes in Operating CANDU Reactors. Internal report of CANDU Owners Group (COG) COG Report No. COG-96–651, Revision 0.

[7] Smith, E. (1996). Threshold stress criterion for delayed hydride crack initiation at a blunt notch in zirconium alloys. *International journal of pressure vessels and piping*, 68, 53–61.

[8] Smith, E. (1967). Fracture initiation at a sharp notch. In *Proceedings of the Royal Society of London A: Mathematical, Physical and Engineering Sciences* (Vol. 299, No. 1459, pp. 455-463). The Royal Society.

[9] Smith, E. (2007). The effect of flaw shape on fracture initiation at a blunt flaw. *Journal of materials science*, 42(1), 307-313.

[10] Scarth, D. A. and Smith, T. (2001). Developments in flaw evaluation for CANDU reactor Zr-Nb pressure tubes. *Journal of pressure vessel technology*, 123(1), 41-48.

[11] Scarth, D.A. and Smith, E. (2002). The effect of plasticity on process zone predictions of DHC initiation at a flaw in CANDU reactor Zr–Nb pressure tubes. *Proceedings of the 2002 ASME Pressure Vessels and Piping Conference*, 437, 19-30.

[12] Canadian Standards Association. (2015). CSA N285.8-15-Technical Requirements for In-Service Evaluation of Zirconium Alloy Pressure Tubes in CANDU Reactors.

[13] Sagat, S., Lee, W. K., and Bowden, J. W., (1994), Atomic Energy of Canada Ltd., Chalk River Laboratories, and Ontario Hydro Technologies, unpublished work, Dec.

[14] Sagat, S., Shi, S.Q., and Puls, M.P. (1994). Crack initiation criterion at notches in Zr-2.5 Nb alloys. *Materials Science and Engineering: A*, 176(1), 237-247.

[15] Cui, J., Shek, G. K., Scarth, D. A., and Wang, Z. (2009). Delayed Hydride Cracking Initiation at Notches in Zr-2.5 Nb Alloys. *Journal of Pressure Vessel Technology*, 131(4), 041407.

[16] Neuber H (1958) *Theory of notch stresses*. Springer, Berlin

[17] Seweryn, A. (1994). Brittle fracture criterion for structures with sharp notches. *Engineering Fracture Mechanics*, *47*(5), 673-681.

[18] Chen, D. H. (1994). Stress intensity factors for V-notched strip under tension or in-plane bending. *International journal of fracture*, *70*(1), 81-97.

[19] Strandberg, M. (1999). A numerical study of the elastic stress field arising from sharp and blunt V-notches in a SENT-specimen. *International Journal of Fracture*, *100*(4), 329-342.

[20] Filippi, S., Lazzarin, P. and Tovo, R. (2002). Developments of some explicit formulas useful to describe elastic stress fields ahead of notches in plates. *International Journal of Solids and Structures*, *39*(17), 4543-4565.

[21] Lazzarin, P. and Filippi, S. (2006). A generalized stress intensity factor to be applied to rounded V-shaped notches. *International journal of solids and structures*, 43(9), 2461-2478.

[22] Savruk, M. P. and Kazberuk, A. (2010). Two-dimensional fracture mechanics problems for solids with sharp and rounded V-notches. *International journal of fracture*, *161*(1), 79-95.

[23] Savruk, M. P. and Kazberuk, A. (2017). *Stress Concentration at Notches*. Springer, Switzerland.

[24] Savruk, M. P. (1981). Two-Dimensional Problems of Elasticity for Cracked Bodies [in Russian], Naukova Dumka, Kyiv.

[25] Benthem, J. P. (1987). Stresses in the region of rounded corners. *International journal of solids and structures*, *23*(2), 239-252.

[26] Metzger, D. R., and Sauvé, R. G. (1996). A self-induced stress model for simulating hydride formation at flaws (No. CONF-960706--). American Society of Mechanical Engineers, New York.

[27] Xu, S. X., Kawa, D., Cui, J., and Chaput, H. (2016). Validation of Weight Function Based Process-Zone Model for Evaluation of Delayed Hydride Cracking Initiation in Zr-2.5 Nb Pressure Tubes. *In ASME 2016 Pressure Vessels and Piping Conference* (pp. V01AT01A054-V01AT01A054).

[28] Seweryn, A., Molski, K. (1996). Elastic stress singularities and corresponding generalized stress intensity factors for angular corners under various boundary conditions. *Engineering Fracture Mechanics*, *55*(4), 529-556.

[29] Williams, M. L. (1952). Stress singularities resulting from various boundary conditions. *Journal of applied mechanics*, *19*(4), 526-528.

[30] Lazzarin, P. and Tovo, R. (1996). A unified approach to the evaluation of linear elastic stress fields in the neighborhood of cracks and notches. *International Journal of Fracture*, 78(1), 3-19.

[31] Dugdale, D. S. (1960). Yielding of steel sheets containing slits. *Journal of the Mechanics and Physics of Solids*, *8*(2), 100-104.

[32] Bilby, B. A., Cottrell, A. H., and Swinden, K. H. (1963). The spread of plastic yield from a notch. *Proceedings of the Royal Society of London A: Mathematical, Physical and Engineering Sciences*, *272*(1350), 304-314.

[33] Gross, D., and Seelig, T. (2011). *Fracture mechanics: with an introduction to micromechanics*. Springer Science & Business Media.

[34] Cui, J. "FC VSR Constant Load DHC Database R2", Kinectrics, Inc., unpublished work.

[35] Tada, H., Paris, P. C., and Irwin, G. R., 2000, *The Stress Analysis of Cracks Handbook*, 3rd ed., ASME, New York.

[36] ANSYS, Ansys 16.0 release documentation. *Theory and modelling guide*. Canonsburg, PA,

USA: ANSYS Inc.